Modeling the dynamics of the inner magnetosphere during strong geomagnetic storms

N. A. Tsyganenko

Universities Space Research Association and Laboratory for Solar and Space Physics, NASA Goddard Space Flight Center, Greenbelt, Maryland, USA

M. I. Sitnov

Institute for Research in Electronics and Applied Physics, University of Maryland, College Park, Maryland, USA

[1] This work builds on and extends our previous effort (Tsyganenko et al., 2003) to develop a dynamical model of the storm-time geomagnetic field in the inner magnetosphere, using space magnetometer data taken during 37 major events in 1996–2000 and concurrent observations of the solar wind and interplanetary magnetic field (IMF). The essence of the approach is to derive from the data the temporal variation of all major current systems contributing to the distant geomagnetic field during the entire storm cycle, using a simple model of their growth and decay. Each principal source of the external magnetic field (magnetopause, cross-tail current sheet, axisymmetric and partial ring currents, and Birkeland current systems) is driven by a separate variable, calculated as a time integral of a combination of geoeffective parameters $N^\lambda V^\beta B_s^\gamma$, where N, V, and B_s are the solar wind density, speed, and the magnitude of the southward component of the IMF, respectively. In this approach we assume that each source has its individual relaxation timescale and residual quiet-time strength, and its partial contribution to the total field depends on the entire history of the external driving of the magnetosphere during a storm. In addition, the magnitudes of the principal field sources were assumed to saturate during extremely large storms with abnormally strong external driving. All the parameters of the model field sources, including their magnitudes, geometrical characteristics, solar wind/IMF driving functions, decay timescales, and saturation thresholds, were treated as free variables, and their values were derived from the data. As an independent consistency test, we calculated the expected Dst variation on the basis of the model output at Earth's surface and compared it with the actual observed Dst. A good agreement (cumulative correlation coefficient $R = 0.92$) was found, in spite of the fact that ~90% of the spacecraft data used in the fitting were taken at synchronous orbit and beyond, while only 3.7% of those data came from distances $2.5 \leq R \leq 4\ R_E$. The obtained results demonstrate the possibility to develop a truly dynamical model of the magnetic field, based on magnetospheric and interplanetary data and allowing one to reproduce and forecast the entire process of a geomagnetic storm, as it unfolds in time and space.

1. Introduction

[2] In our earlier paper [*Tsyganenko et al.*, 2003] (hereinafter referred to as TSK03), a model of the inner magnetospheric storm-time field was described, based on space magnetometer and solar wind plasma data covering 37 storms with $Dst \leq -65$ nT between October 1996 and November 2000. The goal of the present work is to extend that study by taking into account in a physically more consistent way the complex response of the magnetosphere to the external driving during stormy periods. As discussed by TSK03 and many previous authors (e.g., a review by *Gonzalez et al.* [1994]), the geomagnetic storms are intrinsically dynamical events, in which not only the current solar wind and interplanetary magnetic field (IMF) conditions matter, but also the magnetospheric inertia and "memory" effects, reflecting a finite response time, loading/unloading processes, and dissipation of energetic particles trapped

on the inner drift shells. TSK03, as in an earlier work [*Tsyganenko*, 2002a, 2002b] (hereinafter referred to as T02a and T02b), attempted to empirically model the delayed reaction of the magnetosphere to changing solar wind and IMF conditions. To that end, all "partial" components of the total external field (but the magnetopause contribution) were parameterized by the sliding time averages of geo-effective solar wind characteristics calculated over the preceding 1-hour interval, instead of using only their concurrent values, as was done earlier [*Tsyganenko*, 1996]. The averaging smoothed out fast and abrupt variations of the external input and resulted in a more gradual variation of the model field, with a characteristic rise/decay timescale on the order of 1 hour, comparable with the observed magnetospheric response time.

[3] However, the simple averaging adopted by T02 and TSK03 ignored the fact that different sources of the geomagnetic field have widely different response and decay times. While the storm-time symmetric ring current requires at least several hours to build up and decays on the timescale of at least one or two days, the magnetotail current varies much faster. A typical reaction time of the tail lobe field to the solar wind pressure pulses is only a few minutes [*Collier et al.*, 1998], even though its response to the onset of southward IMF B_z has a longer timescale, up to 2–3 hours [*Caan et al.*, 1975].

[4] Another limitation of the above models was a somewhat haphazard choice of the geoeffective solar wind drivers. In the TSK03 model we used ad hoc indices G_2 and G_3, calculated as hourly averages $\langle VB_s \rangle$ and $\langle NVB_s \rangle$, respectively, but no attempt was made to try more general combinations and see if they yield better results.

[5] All the above motivated us to look for a more accurate and physically consistent approach, in which each source of the magnetic field would have its own relaxation timescale and a driving function, based on an individual best fit combination of the solar wind and IMF parameters. This paper presents a model of the storm-time inner geomagnetic field, driven by the upstream solar wind data. Mathematically, the model has a modular structure similar to that used by T02 and uses the same approximations for the individual magnetic field modules, systematically described by T02a and more briefly overviewed by TSK03. Also, the data used in this work is essentially the same 37-storm data set described in detail by TSK03, which allows us to shorten the paper and concentrate on the essence of the new approach. Readers interested in more details of the model's mathematical specifics and the data are referred to the earlier publications.

[6] An entirely new element in this work is the way of parameterizing the model by the dynamical solar wind input. Previous efforts were focused mainly on the spatial structure of the distant geomagnetic field, whose inherent complexity called for more and more sophisticated approximations. In the modeling of the storm-time magnetosphere, however, the temporal behavior of individual field sources comes to the forefront. It was not paid proper attention in earlier data-based models, since they were intended mostly for describing the average magnetosphere under specific solar wind or geomagnetic conditions. That approach is no longer valid in the modeling of the storm-time field, in this case both the spatial structure and its time evolution become equally important.

2. Approach

[7] When constructing an empirical magnetospheric model, we start from devising simple "modules" having physically realistic and flexible spatial structure, represent the total field as a superposition of these modules, and fit that field to a large set of data covering a sufficiently wide region in the geometrical and parametrical space. In doing so, it is implicitly assumed that the state of the magnetosphere is a reasonably predictable function of the solar wind state, in other words, under similar external conditions one can expect nearly the same configuration of the distant geomagnetic field.

[8] This work is based on essentially the same premise, but also with respect to the time variation of the magnetosphere. It is assumed that similar initial conditions and the same history of the external driving result in nearly the same response of the magnetospheric currents and hence the same temporal evolution of the field configurations.

[9] We need first to choose a simple and sufficiently flexible model of the response of the principal field sources to the external driving. It seems reasonable to start with an assumption that, in general, each magnetospheric current system has two types of response to the external driving. The first one is usually related to variations of the solar wind pressure, rapidly propagating via Alfven waves inside the magnetosphere. On the timescale of a storm, this is a virtually instantaneous reaction, which can be easily reproduced, for example, by including an appropriate pressure-dependent factor in the size of the magnetopause and the related strength of the Chapman-Ferraro field. The second type of response is associated with slower processes, such as the reconnection at the magnetopause, plasma convection, particle losses due to pitch angle diffusion and charge exchange, etc. These effects can be empirically modeled by including a term W in the total strength of a field source, whose magnitude behaves in time according to the equation

$$\frac{\partial W}{\partial t} = S - L, \tag{1}$$

where the quantities S and L in the right-hand side are the source and loss functions, respectively. The source term S represents the feeding rate of a current system by the solar wind input, which can be empirically assumed as a function of the external driving factors, for example, having the form

$$S = aN^\lambda V^\beta B_s^\gamma, \tag{2}$$

where N and V are the solar wind density and speed, B_s is the southward component of the IMF, and the coefficient a and the power indices λ, β, and γ are unknown parameters of the driving function.

[10] The loss term L in (1) can have a different physical meaning, depending on which current system is being considered. Its interpretation is the most straightforward for the symmetrical part of the ring current, in which case it

is closely related to the rate of the dissipation of energetic particles due to their pitch angle and radial diffusion, as well as charge exchange processes. In the spirit of the approach by *Burton et al.* [1975] and other studies of the *Dst* field dynamics [e.g., *Gonzalez et al.*, 1994, and references therein], one can assume the loss term L to be proportional to the difference between the current value of W and its residual quiet-time level W_0, so that

$$L = r(W - W_0), \qquad (3)$$

which yields a simple solution

$$W(t) = W_0 + \int_0^t S(\tau) \exp[r(\tau - t)] d\tau, \qquad (4)$$

where r is the decay rate and the integration is made from the beginning of the event $\tau = 0$ to the current moment $\tau = t$. Dynamical models similar to (1)–(3) were used earlier in a number of works to describe global loading-unloading processes in storms [*Burton et al.*, 1975; *Temerin and Li*, 2002] and substorms [*Baker et al.*, 1990; *Klimas et al.*, 1992; *Horton and Doxas*, 1996].

[11] In this work, we extend this simple formalism to describe the dynamics of all major sources of the magnetospheric field, including the partial ring current, cross-tail current, and Birkeland currents. Even though one might speculate on the physical nature of the loss term for these current systems and dispute the validity of the assumed linear dependence of the loss rate L on W in (3), in fact, that assumption is not critical here. Formally, the decay rate r can be considered just as an inverse measure of the relaxation timescale $T = 1/r$ (or "inertia") of a given field source, regardless of its physical interpretation. Larger (smaller) values of r provide a faster (slower) reaction of the magnetospheric current to an external disturbance and its quicker (more gradual) return to the quiet-time level after the driving force disappears. Our goal here is to derive from the data best fit estimates of the decay rate for individual current systems and compare them with those based on intuitively expected relaxation timescales. We concentrate here on a large-scale description of the storm-time evolution of the magnetospheric currents, and leave out more short-lived phenomena, including substorms. More discussion of these aspects will be given in section 5.

3. Overview of the Model Field Approximation

[12] Following the general approach presented in detail by T02 and TSK03, the external model field is approximated by a linear combination of seven vectors: (1) the Chapman-Ferraro field $\mathbf{B}_{CF}$, confining the Earth's internal field within the magnetopause, (2) the tail field $\mathbf{B}_T$, (3) the field $\mathbf{B}_{SRC}$ of a symmetrical ring current, (4) the field of a partial ring current $\mathbf{B}_{PRC}$, (5)–(6) the fields of the Region 1 and 2 Birkeland current systems, and (7) a penetrated component of the IMF given by an "interconnection" term $\mathbf{B}_{int} = \varepsilon \mathbf{B}_\perp^{IMF}$.

[13] An exhaustive systematic description of the model field components was given by T02a, and the page limits of this paper do not permit us to fully reproduce it here. To help the reader understand the main principles of the model without going back to our earlier publications, a concise overview of each field source is given below, in which we concentrate mostly on the underlying physical assumptions and their validity, leaving out tedious mathematical details.

[14] The approximation for the Chapman-Ferraro field, $\mathbf{B}_{CF}$, is constructed as a flexible combination of curl-free fields, based on the gradients of scalar potentials having the form

$$\exp\left(X\sqrt{\frac{1}{p^2} + \frac{1}{q^2}}\right) \cos\frac{Y}{p} \begin{Bmatrix} \sin(Z/q) \\ \cos(Z/q) \end{Bmatrix}.$$

The above potentials were used as basis functions in an expansion, with the corresponding weight coefficients and the nonlinear scaling parameters p and q being found by least squares, to minimize the RMS residual normal component $\langle B_n^2 \rangle$ over a set of points, distributed over the model magnetopause up to a tailward distance of 70 R_E. The total number of terms in the expansion was chosen equal to 18, which yielded a virtually perfect shielding of the Earth's dipole inside the model magnetopause, within the full observed range of the dipole tilt angles. More details on this are given by T02a (section 2.4.1).

[15] The tail field, $\mathbf{B}_T$, was represented using previously developed analytical approximations, corresponding to equatorial current sheets with finite variable thickness. The current density in such a sheet is vanishingly small near Earth, but rapidly rises with growing distance, peaks near the observed position of the inner edge of the cross-tail current, and then gradually decreases further tailward, in accordance with the observed average gradient of the tail lobe field. The tail field also included a shielding component, represented by a combination of the potential fields, mathematically similar to the above harmonics used in the term $\mathbf{B}_{CF}$. The effects of the dipole tilt on the shape of the cross-tail current were taken into account using the deformation technique, as described in full detail by T02a (section 2.2). To make the nightside tail field more flexible, we further expanded the tail term $\mathbf{B}_T$ into a linear combination of two fields, $\mathbf{B}_{T1}$ and $\mathbf{B}_{T2}$ with different spatial variation scales along the tail axis, corresponding to the inner and outer parts of the cross-tail current, respectively.

[16] As said above, the contribution from the ring current was split into two parts, corresponding to its axially symmetric component, $\mathbf{B}_{SRC}$, and the partial ring current field, $\mathbf{B}_{PRC}$, including the effect of the field-aligned currents associated with the local time asymmetry of the azimuthal near-equatorial current. The approximations for the magnetic field were derived in our earlier work [*Tsyganenko*, 2000b] on the basis of the observed profiles of the particle pressure and anisotropy, according to the data of *Lui and Hamilton* [1992]. The reader is referred to those papers for more details and mathematical specifics.

[17] The contributions from Birkeland currents use the approximations, developed and described in detail by T02a. The approach is based on the so-called "conical" model [*Tsyganenko*, 1991] of the magnetic field, corresponding to a distribution of radial currents flowing on a conical surface that intersects Earth along a circle of constant geomagnetic latitude. As shown by T02a, the conical model cannot be

used in its original form, since the radial currents are grossly different in their geometry from the actual Birkeland currents, flowing in the inner magnetosphere along quasi-dipolar field lines. That inconsistency was removed by T02a by applying a deformation of coordinates, bringing the model into much closer agreement with the expected distribution of the currents, based on a more realistic shape of their flow lines. It also should be noted that in work by T02a, T02b, and TSK03 the contributions from the Region 1 and 2 Birkeland current systems were split into sums of two terms, in which the first one represented the principal mode, proportional to the sine of the longitude ϕ (so that the corresponding field-aligned current at low altitudes peaks at dawn and dusk). Inclusion of the second term, proportional to $\sin 2\phi$, made it possible to shift the current peaks toward noon or midnight (see T02a, section 2.3 and Figure 5, for more details). In this study, similar bimodal expansions were initially adopted for the field of field-aligned currents. However, the magnitudes of the second harmonics were a posteriori found to be much smaller than for the principal modes, both for the Region 1 and 2 modules. For that reason, they were left out in the final approximation.

[18] Each of the above vectors entering in the total model field (but $\mathbf{B}_{CF}$) is normalized, separately shielded inside the model magnetopause, and multiplied by a scalar coefficient, representing the magnitude of each source as a function of the current state of the interplanetary medium and of the previous history of the external driving, so that the total field of the magnetospheric sources has the form

$$\mathbf{B}^{(\mathrm{mod})} = \mathbf{B}_{CF} + t_1 \mathbf{B}_{T1} + t_2 \mathbf{B}_{T2} + s \mathbf{B}_{SRC} + p \mathbf{B}_{PRC} + b_1 \mathbf{B}_{R1}$$
$$+ b_2 \mathbf{B}_{R2} + \varepsilon \mathbf{B}_\perp^{\mathrm{IMF}}. \tag{5}$$

The Chapman-Ferraro field $\mathbf{B}_{CF}$ confines the Earth's field inside the magnetopause; it is fully defined by the strength and tilt angle of the Earth's dipole and by the shape and size of the boundary. The magnetopause is a predefined surface, fitted to the empirical boundary of *Shue et al.* [1998] but, in contrast to the original model, it is controlled only by the solar wind ram pressure (see section 3.1 by TSK03 for details).

[19] The magnitude coefficients in (5) were represented as

$$t_1 = t_1^{(0)} + t_1^{(1)} W_{t1} / \sqrt{1 + (W_{t1}/W_{t1c})^2} + t_1^{(2)} (P_d/P_{d0})^{\alpha_1}$$

$$t_2 = t_2^{(0)} + t_2^{(1)} W_{t2} / \sqrt{1 + (W_{t2}/W_{t2c})^2} + t_2^{(2)} (P_d/P_{d0})^{\alpha_2}$$

$$s = s^{(0)} + s^{(1)} W_s / \sqrt{1 + (W_s/W_{sc})^2}$$

$$p = p^{(0)} + p^{(1)} W_p / \sqrt{1 + (W_p/W_{pc})^2} \tag{6}$$

$$b_1 = b_1^{(0)} + b_1^{(1)} W_{b1} / \sqrt{1 + (W_{b1}/W_{b1c})^2}$$

$$b_2 = b_2^{(0)} + b_2^{(1)} W_{b2} / \sqrt{1 + (W_{b2}/W_{b2c})^2},$$

where the solar wind ram pressure P_d was normalized by its average quiet-time value $P_{d0} = 2$ nPa, and the driving variables W_{t1}, W_{t2}, W_s, W_p, W_{b1}, W_{b2}, and their respective saturation levels W_{t1c}, W_{t2c}, W_{sc}, W_{pc}, W_{b1c}, W_{b2c} are discussed below.

[20] As already said, the rationale behind adding the pressure-dependent terms in the coefficients t_1 and t_2 in (6) is that the response of the tail field to the solar wind and IMF variations includes both instantaneous and delayed components. It is well established [e.g., *Collier et al.*, 1998] that the tail lobe field variations almost immediately respond to changes in the solar wind pressure, while the IMF effects in the same field can significantly lag the external input [*Tsyganenko*, 2000a]. In general, the functional forms in (6) resemble those assumed by TSK03. The important difference, however, is in the terms containing the variables W, each of which is defined here as

$$W(t_i) = \frac{r}{12} \sum_{k=1}^{i} S_k \exp\left[\frac{r}{60}(t_k - t_i)\right], \tag{7}$$

where

$$S_k = \left(\frac{N_k}{5}\right)^\lambda \left(\frac{V_k}{400}\right)^\beta \left(\frac{B_{sk}}{5}\right)^\gamma. \tag{8}$$

Equation (7) is just an equivalent of the integral in the right-hand side of (4), in which the integration is replaced by summation over 5-min intervals from the beginning of a storm at $t = t_1$ to the current moment $t = t_i$. In (7) we assume the inverse timescale r (relaxation rate) to be measured in hours^{-1}, while the time t is in minutes; this explains the factors 1/12 and 1/60. In addition, to avoid too large values of the variables W, they are normalized by including in the right-hand side of (7) the relaxation rate r as a common factor. For the same reason, the values of the solar wind density N_k, speed V_k, and the magnitude of the southward IMF component B_{sk} in (8) are divided by their characteristic order-of-magnitude values.

[21] Thus defined variables W enter in the 6 magnitude coefficients in (6), each one having its own relaxation rate r and a driving function S with individual set of power indices λ, β, and γ. In all the equations (6) the variables W enter via nonlinear forms $W/\sqrt{1 + (W/W_c)^2}$, implying a linear response for a weak external driving, but a gradual saturation during strongly disturbed periods when W exceeds its threshold level W_c. TSK03 introduced similar nonlinear terms to describe the saturation of the tail, Birkeland, and partial ring current. In that work we used only two indices G_2 and G_3, based on a tentative single choice of the driving parameters, averaged over 1-hour interval prior to the current moment. Here, in contrast, a set of 6 individual dynamical variables W is employed, defined by semiempirical equations (1)–(4) and calculated using the entire record of the solar wind and IMF conditions during each of the 37 storms.

[22] In an early version of this model (as well as in work by T02a, T02b, and TSK03), the tail and ring current coefficients t_1, t_2, s, and p in (6) also contained in their right-hand side terms proportional to the corrected $Dst^* = 0.8\,Dst - 13\sqrt{P_d}$. Even though the presence of those terms brought a slight improvement to the least squares fit, they were eventually removed as mostly redundant. That decision was motivated by the fact that the Dst^* combines the effects of several sources, in which the ring and tail currents are principal contributors and whose dynamics, causally

related to the external conditions, is already represented in the right-hand side of (6) by the terms with the driving parameters W. In addition, relative contributions of these sources to the Dst are quite different during the main and recovery phases of a storm, which would require time-dependent weight coefficients by Dst^*. Note that, even though the linear dependence on Dst^* was abandoned in (6), it was still used as a nonlinear parameter, controlling the variable position of the cross-tail current sheet along the tail axis, as described below in more detail.

[23] A larger flexibility of the inner tail field was achieved in this model by introducing a variable thickness and a shift of the current sheet along the tail axis, parameterized by the corresponding solar wind driving function W_{t1} and Dst^*. The purpose of the modification was to replicate the observed formation of a very intense and thin current sheet in the nightside inner magnetosphere, reconfiguring the prestorm quasi-dipolar field in such a way that it becomes essentially tail-like even at synchronous distance [*McPherron*, 1972; *Kaufmann*, 1987]. Owing to the large percentage in the data set of GOES 8, 9, and 10 nightside observations, we expected that feature to be conclusively resolved by the fitting algorithm. The half-thickness D of the tail current sheet was approximated as

$$D = D_0 + D_1 \exp(-\delta\, W_{t1}), \qquad (9)$$

so that $D_0 + D_1$ yields the half-thickness at quiet times, and δ defines its sensitivity to the solar wind driving, represented by the same function W_{t1} that enters in the first equation in (6) for the amplitude of the inner tail current. Positive values of δ correspond to a thinning of the current sheet, once the magnetosphere gets exposed to the southward IMF B_z and the parameter W_{t1} starts growing. As discussed in the next section, fitting of the model to the data yielded an estimate for δ that clearly indicated the expected effect.

[24] Additional degrees of freedom were introduced by allowing both tail current sheets (i.e., the inner and outer tail field modules) to shift along the tail axis with respect to their quiet-time positions. The shifts were assumed as simple functions of Dst^*:

$$\Delta X_{1,2} = \Delta X_{1,2}^{(0)} - \frac{\Delta X_{1,2}^{(1)}}{[\max\{20, |Dst^*|\}]^\gamma}, \qquad (10)$$

so that larger values of $|Dst^*|$ would result in earthward/tailward shifts for positive/negative $\Delta X_{1,2}^{(1)}$. Starting values of the parameters in (10) were specified by assuming that the spatial extent of plasma intrusion into the inner magnetosphere is proportional to the earthward shift of the contours of equal B, caused by the deepening of the magnetic depression during a storm. Interpreting Dst^* as a crude measure of that depression and assuming a purely dipolar Earth's field ($B \sim R^{-3}$), one obtains $\gamma \sim 1/3$ for the power index in (10). This in turn yields a rough estimate $\Delta X_{1,2}^{(1)} \sim 20$, based on an obvious fact that even during a very strong storm with $Dst^* \sim -300$ nT, the maximum earthward shift of the current sheet from its quiet-time position (say, from $X \sim -8\ R_E$ at $Dst^* \sim -20$) cannot exceed $3-5\ R_E$. The best fit values of $\Delta X_1^{(0)}$ and $\Delta X_1^{(1)}$ for the inner tail field

did not deviate too much from the above estimates, but the outer current sheet was found to move within a wider range of X, as described in more detail in the next section.

[25] In general, the derivation of the model parameters by least squares was based on procedures used in our earlier studies. All variable parameters were divided into two groups, linear coefficients $\{A_i\}$ and nonlinear parameters $\{Q_i\}$. The optimization search was made in the space of nonlinear parameters $\{Q_i\}$ using the downhill simplex method [*Press et al.*, 1992], while the values of the coefficients $\{A_i\}$ at each step were calculated by a standard inversion algorithm.

[26] The linear parameters included 14 coefficients in the right-hand side of (6) and the IMF penetration coefficient ε in (5). The 49 nonlinear parameters included two power indices α_1 and α_2, 17 variables defining the geometrical characteristics of the field sources and their variation with the disturbance level, 6 relaxation rates (for each of the 6 variables W entering in (6)), 18 power indices λ, β, and γ entering in the right-hand side of (8) (3 for each of the 6 modules), and 6 saturation levels W_c. Initial values of the nonlinear parameters were based in most cases on tentative order-of-magnitude guesses. All the 6 relaxation rates r_i were initially assumed equal to 0.5, implying an average relaxation time of 2 hours. The initial values of the saturation levels W_c were set equal to the characteristic peak values of each corresponding driving variable W.

[27] Because of the large number of variable nonlinear parameters, they were divided into two groups and the iterative search was made alternately, by varying the parameters in only one group at a time, while those in the other one remained fixed. Using that method was dictated by two reasons. First, the efficiency of the downhill simplex algorithm significantly deteriorated with the growing number of variable parameters. The second reason was the "integral" nature of the 6 variables W, entering in the amplitude coefficients of the field sources in (6). All previously developed fitting algorithms assumed either instantaneous response of a magnetospheric field source to the solar wind conditions, or used precalculated averages of the driving parameters over preceding time intervals with a fixed length. Here, in contrast, each of the 6 variables W is represented by the sum (7) over the entire sequence of the solar wind data, from the beginning of each storm to a current time moment, and that summation must be redone at each iterative step, since the result depends on the values of the relaxation rates r_i and the parameters λ_i, β_i, and γ_i in the driving functions, which vary from one iteration to the next. All this resulted in quite a computationally intensive procedure, and special measures were taken to optimize the calculation.

4. Results

[28] As said before, this work used the same set of 5-min average data as in work by TSK03, based on 37 storms in 1996–2000, each of which was fully covered by a continuous sequence of the solar wind/IMF data. That made it possible to calculate for each magnetospheric data record the corresponding values of the variables $W(t_i)$, defined by (7). The total number of data records in the set was 142,787, of which $\sim$23% corresponded to locations $7 \le R \le 20\ R_E$,

Table 1. Best Fit Values of the Tail Field Parameters Entering in (5)–(8)

$\mathbf{B}_{t1}$		$\mathbf{B}_{t2}$	
Parameter	Value	Parameter	Value
$t_1^{(0)}$	5.2 ± 0.2	$t_2^{(0)}$	-6.5 ± 1.5
$t_1^{(1)}$	8.7 ± 0.6	$t_2^{(1)}$	-3.85 ± 0.5
$t_1^{(2)}$	0.9 ± 0.2	$t_2^{(2)}$	11.3 ± 1.5
α_1	0.74 ± 0.13	α_2	0.23 ± 0.02
λ_{t1}	0.39 ± 0.03	λ_{t2}	0.46 ± 0.20
β_{t1}	0.80 ± 0.04	β_{t2}	0.18 ± 0.1
γ_{t1}	0.87 ± 0.03	γ_{t2}	0.67 ± 0.1
W_{t1c}	0.71 ± 0.05	W_{t2c}	0.39 ± 0.05
r_{t1}	0.39 ± 0.01	r_{t2}	0.7 ± 0.1

$\sim$68% came from a relatively narrow interval of radial distances $6 \leq R \leq 7\ R_E$ (with the largest contribution from synchronous GOES 8, 9, and 10 spacecraft), $\sim$5.3% of data were taken at $4 \leq R \leq 6\ R_E$, and only 3.7% fell in the innermost range $2.5 \leq R \leq 4\ R_E$. The RMS value of the observed external field $\mathbf{B}_e$ (i.e., with the IGRF model field subtracted) over the entire set was 45.6 nT, and the residual RMS deviation of the best fit model field from $\mathbf{B}_e$ was found equal to $\sigma = 17.70$ nT.

[29] Tables 1, 2, and 3 present the results of the least squares fitting of the model to the data. Table 1 contains the values of coefficients and nonlinear parameters for the first two tail field modules, $\mathbf{B}_{t1}$ and $\mathbf{B}_{t2}$, specified in (5)–(8). Table 2 corresponds to the magnetic field of the symmetrical and partial ring current, $\mathbf{B}_{SRC}$ and $\mathbf{B}_{PRC}$, and Table 3 provides the parameters for the region 1 and 2 field-aligned current modules $\mathbf{B}_{R1}$ and $\mathbf{B}_{R2}$, entering in (5). Using typical values of the driving parameters entering in (6) and the coefficients in Tables 1−3, one can estimate the range of variation of the magnitudes of individual field sources in (5). In view of the complexity of the calculation of the integral variables W_i, defined in (7) and (8), we provide here their peak estimates, based on five largest storms in our database: $W_{t1} \sim 4$−12, $W_{t2} \sim 3$−7, $W_s \sim 4$−15, $W_p \sim 10$−50, $W_{b1} \sim 7$−30, and $W_{b2} \sim 20$−100.

[30] The first fact clearly evident from Table 1 is the increase of the distant tail field with growing solar wind ram pressure P_d, in agreement with all previous statistical and modeling studies [e.g., *Fairfield and Jones*, 1996; *Tsyganenko*, 2000a, 2002b]. Using the obtained values of $t_1^{(0)}, t_1^{(2)}, t_2^{(0)}, t_2^{(2)}, \alpha_1$, and α_2, one can see that a fivefold rise in the pressure from 2 to 10 nPa results in the increase of the coefficients t_1 and t_2 in (5) by the factors 1.35 and 2.0, respectively (assuming a northward IMF and hence zero contribution from the IMF-related terms). Note that the more distant part of the tail is much more sensitive to the

Table 2. Best Fit Values of the Ring Current Parameters Entering in (5)–(8)

$\mathbf{B}_{SRC}$		$\mathbf{B}_{PRC}$	
Parameter	Value	Parameter	Value
$s^{(0)}$	0.56 ± 0.04	$p^{(0)}$	0.77 ± 0.03
$s^{(1)}$	0.94 ± 0.07	$p^{(1)}$	0.69 ± 0.06
λ_s	0.39 ± 0.04	λ_p	0.42 ± 0.06
β_s	2.32 ± 0.15	β_p	1.25 ± 0.2
γ_s	1.32 ± 0.03	γ_p	1.29 ± 0.1
W_{sc}	3.3 ± 0.5	W_{pc}	75 ± 30
r_s	0.031 ± 0.003	r_p	0.58 ± 0.08

**Table 3.** Best Fit Values of the Birkeland Current Parameters Entering in (5)–(8)

$\mathbf{B}_{R1}$		$\mathbf{B}_{R2}$	
Parameter	Value	Parameter	Value
$b_1^{(0)}$	0.32 ± 0.03	$b_2^{(0)}$	-0.04 ± 0.02
$b_1^{(1)}$	1.23 ± 0.04	$b_2^{(1)}$	-0.38 ± 0.02
λ_{b1}	0.41 ± 0.02	λ_{b2}	1.29 ± 0.04
β_{b1}	1.6 ± 0.2	β_{b2}	2.4 ± 0.3
γ_{b1}	0.69 ± 0.03	γ_{b2}	0.53 ± 0.04
W_{b1c}	6.4 ± 1.0	W_{b2c}	4.44 ± 0.5
r_{b1}	1.15 ± 0.06	r_{b2}	0.88 ± 0.06

solar wind pressure, even though the corresponding power index $\alpha_2 = 0.23$ is roughly three times smaller than $\alpha_1 = 0.74$ for the inner tail module. The obtained dependence of the distant field on the pressure $t_2 = -6.45 + 11.3(P_d/2)^{0.23}$ is in a good agreement with the result of Fairfield and Jones (see their equation (4)), with their power index also being close to 0.25.

[31] The IMF-related effect in the tail field is quantified by the second terms in the right-hand side of the first two equations in (6). It is quite significant for the inner module $\mathbf{B}_{t1}$, because of the relatively large and positive value of the coefficient $t_1^{(1)}$. As a result, the magnitude t_1 of the inner field substantially increases during periods of strong southward IMF. However, that increase is largely offset because of a relatively low value of the saturation threshold W_{t1c}, which effectively limits the growth of the tail field during strong storms. The outer tail field, quantified by the coefficient t_2, even slightly decreases with the growing driving variable W_{t2} (due to $t_2^{(1)} < 0$), indicating a concentration of the storm-time tail current at progressively closer geocentric distances. In an average sense, the strong saturation of both tail terms manifests an effective discharge of the tail's magnetic energy, rapidly increasing with growing external driving. Finally, note the difference between the decay rates $r_{t1} = 0.39$ and $r_{t2} = 0.70$, corresponding to the relaxation times 2.6 and 1.4 hours for the inner and outer tail modules, respectively. This implies a significantly quicker response of the outer tail current to the onset of southward IMF, which agrees with the expected larger susceptibility of the distant tail to the solar wind control.

[32] Regarding the symmetrical ring current, first of all note a much smaller value of the decay rate ($r_s = 0.031$) in comparison with all other field sources, corresponding to a much longer relaxation time $\tau_s = r_s^{-1} \sim 32$ hours. This significantly exceeds the estimates in the range 5−15 hours, typically obtained in the studies based on the dynamics of the *Dst* index [e.g., *Gonzalez et al.*, 1994; *Valdivia et al.*, 1996]. The most likely reason for the disagreement is an implicit assumption made in the above works that the ring current is the principal contributor to the *Dst*, while all other sources have only minor effect. As has been long argued by *Maltsev* [2004, and references therein], that assumption is inaccurate, because a significant, if not the main, part of the storm-time *Dst*, is due to the tail current. As shown in the next section, our modeling confirms that view, but mostly with respect to the main phase of a storm, in agreement with the results of *Dremukhina et al.* [1999] and *Skoug et al.* [2003]. At the peak of *Dst*, the contributions from both sources are comparable (and the tail field indeed often prevails), but already at the early recovery phase the tail
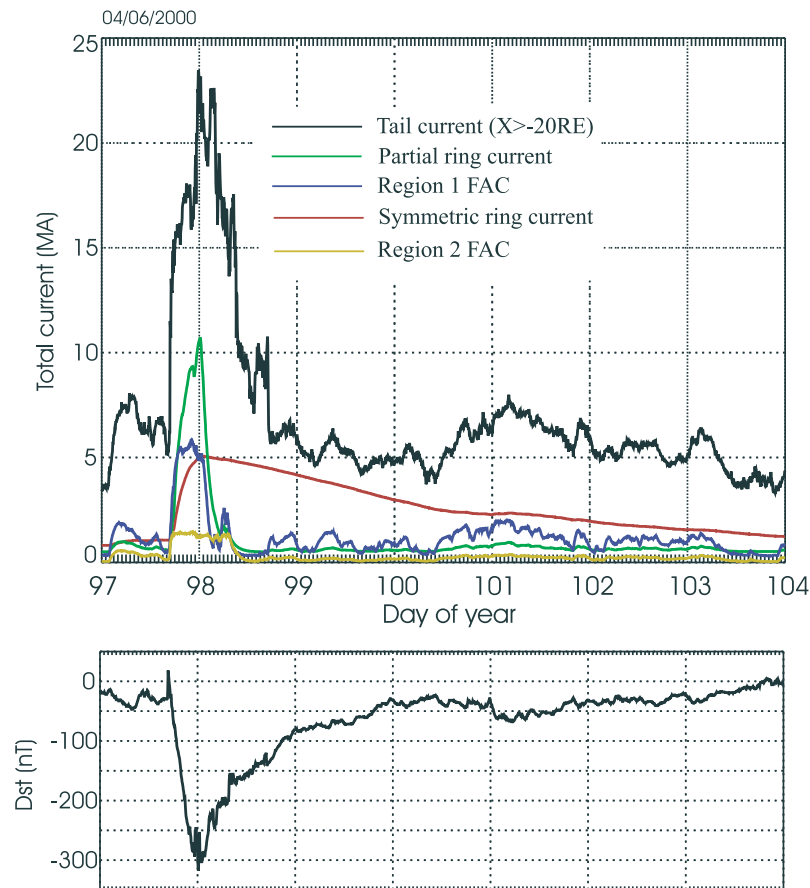
Figure 1. (top) Variation of the total current in the five principal current systems during the storm of 6–10 April 2000. (bottom) Concurrent variation of the *Dst* index during the event.

current rapidly declines, and the contribution of the symmetric ring current becomes dominant in the *Dst* field. It means that, if one attempts to quantify the dynamics of the *Dst* using a single empirical relaxation time τ, its best fit value should be found somewhere between the individual values for the ring and tail currents, which reconciles our result with the earlier empirical estimates.

[33] The behavior of the model partial ring current drastically differs from that of the symmetric ring current, which is readily apparent from its parameters in Table 2. During quiet times (i.e., before a storm, when $W_p = 0$) the partial ring current magnitude is very small, defined by the free term $p^{(0)}$ in the coefficient p. Upon the arrival of the disturbed solar wind with a strong southward IMF, the second term quickly grows, so that at the peak of the main phase the partial ring current significantly exceeds the symmetric one, in line with the simulation results of *Liemohn et al.* [2001]. As demonstrated in those simulations, this is due to a dramatic increase of the magnetospheric convection during the periods with enhanced solar wind driving. In this regard, note the relatively large value of the saturation threshold $W_{pc} = 75$ for the partial ring current, well beyond the range of the corresponding driving parameter W_p. That implies only a weak saturation, even during exceptionally intense storms (like the Bastille Day event of 07/15/2000 with the peak $W_p \approx 54$). Another

noteworthy fact is a much larger decay rate of the partial ring current ($r_p = 0.58$), in comparison with the symmetric one ($r_s = 0.031$), which means that the partial ring current quickly subsides (on a timescale $\tau_p \sim 2$ hours), once the external driver is turned off. More discussion of the temporal variation of all model field sources in individual events will be given below.

[34] According to the adopted normalization of the model field vectors $\mathbf{B}_{R1}$ and $\mathbf{B}_{R2}$ in (5), the numerical values of the coefficients b_1 and b_2 are respectively equal to the total downward region 1 and 2 Birkeland currents per one hemisphere in MA (negative values indicate an upward current). As can be seen from Table 3, the obtained best fit values are in a reasonable agreement with the expected overall magnitude of the field-aligned currents and their response to the solar wind/IMF driving. At quiet conditions with $W_{b1} = W_{b2} = 0$, the amplitude coefficients b_1 and b_2 are equal to 0.32 and -0.04, respectively, corresponding to a relatively weak region 1 and virtually zero region 2 currents. At the moderate level of the solar wind driving with $W_{b1} \sim 3$ and $W_{b2} \sim 10$ (assumed at about half the lower estimates of their storm-time peak values), one obtains $b_1 = 3.6$ and $b_2 = -1.6$, which corresponds to the total downward/upward region 1/region 2 currents equal to 3.6/1.6 MA, respectively. During the periods with extremely strong driving, the nonlinear saturation comes into effect, so that
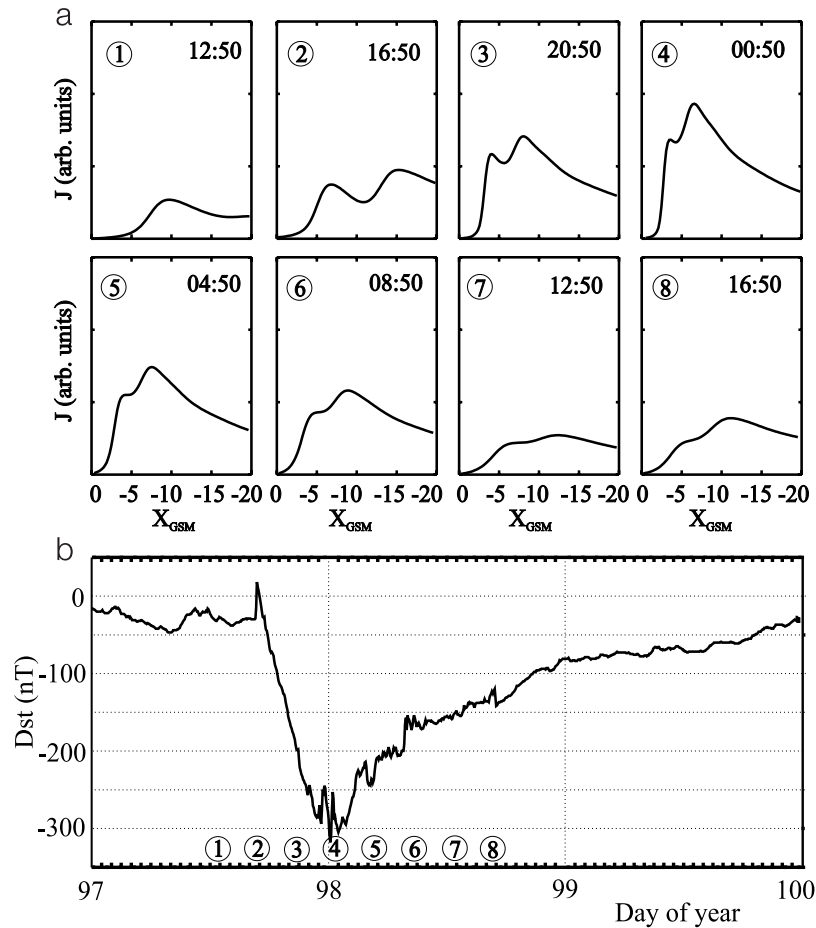
Figure 2. (a) Temporal evolution of the cross-tail current profile along the tail's axis during the storm of 6–10 April 2000. (b) Concurrent *Dst*-variation with the eight consecutive time moments indicated by the circled numbers.

the asymptotic maximal values of the model region 1 and 2 currents are $b_1^{(0)} + b_1^{(1)} W_{1c} = 8.1$ MA and $b_2^{(0)} + b_2^{(1)} W_{2c} = 1.7$ MA, respectively.

[35] With respect to the temporal characteristics of the model field-aligned currents, the region 1 system yielded the largest decay rate $r_{b1} = 1.15$, in comparison to all other sources, and hence the smallest relaxation timescale $\tau_{b1} \sim 52$ min. This is consistent with the notion that the region 1 currents reach the outermost regions of the magnetosphere and connect the ionosphere with the solar wind in the most direct way. The region 2 current was found to have the decay rate $r_{b2} = 0.88$, smaller than that of the region 1, but larger than for the partial ring current, which is what one should expect, taking into account its intermediate location with respect to that of the latter.

[36] The IMF penetration effect was represented in the model in the simplest possible way, assuming a uniform penetrated field and no modulation by the IMF clock angle θ. The latter assumption was based on the earlier result of TSK03 that the penetration, quantified by the coefficient ε, only weakly varied with θ. In this study, the best fit value of the penetration coefficient was found equal to ε = 0.46, in close agreement with the earlier estimate ε = 0.42 of TSK03.

[37] An illustrative way to present the information contained in the model parameters is to analyze the varia-

tion of the total current in each magnetospheric current system during a typical storm. Figure 1 presents the result of calculating the currents in individual sources for a strong storm of 6–10 April 2000 with the peak *Dst* ∼ −300 nT. The five plots in Figure 1 (top) correspond to the total tail current (black), symmetrical ring current (red), partial ring current (green), and region 1 and 2 field-aligned currents (blue and yellow lines, respectively), and Figure 1 (bottom) displays the observed *Dst* variation (based on the 5-min average SYM index). All the currents were calculated by numerically integrating $\nabla \times \mathbf{B}$, corresponding to the individual field sources. Since the tail current is not spatially bounded on the nightside, such an estimate naturally depends on the antisunward extent of the integration area. In our calculation that area was arbitrarily limited to the rectangle $-20\ R_E \leq X_{\mathrm{GSM}} \leq 0$, $|Z_{\mathrm{GSM}}| \leq 5\ R_E$, so that the variation of the tail current in the plot actually corresponds to the near part of the tail. The total partial ring current was calculated by integrating its azimuthal component over the meridian plane MLT = 19:00, where the maximum of the westward current was found to be located. The estimates for the region 1/2 field-aligned currents correspond, respectively, to the total inflowing/ outflowing current (per one hemisphere only), obtained by integration at the ionospheric altitude in the northern hemisphere.

[38] As can be seen from Figure 1, the five current systems largely differ from each other, both with respect to their relative strength and variation timescales, quantified by the respective decay parameters r. The symmetrical ring current rose to its peak magnitude of $\sim$5 MA within 6–7 hours after the storm's sudden commencement and then gradually subsided over the timescale of several days. All the other currents rose and decayed on a much shorter timescale. The total partial ring current rapidly increased and peaked at the maximum of the storm main phase at $\sim$11 MA, which more than twice exceeded the total symmetrical ring current at that time. After the IMF B_z turned northward (shortly after midnight on 7 April), the partial ring current quickly fell off. Note that because of its geometry, the partial ring current makes a relatively small contribution to the ground Dst field; that issue will be addressed in more detail in section 5. The region 1 field-aligned current rapidly rose to its peak value $\sim$6 MA and also quickly subsided after the external driving ended; the subsequent secondary peaks on the plot correspond to transient intervals of a weaker southward IMF during the storm recovery phase.

[39] As already noted, the apparent predominance of the tail current in the plot is largely due to our arbitrary choice of the integration area. A more objective global characteristic of the tail current is its relative contribution to the ground field, discussed in the next section. The model also reveals interesting details of the storm-time redistribution of the tail current, reported earlier in several case studies [Kaufmann, 1987, and references therein]. Specifically, the best fit values of the parameters D_0, D_1, and δ, entering in (9), were found equal to 0.56, 1.94 and 0.57, respectively. This corresponds to a thick and weak prestorm current sheet with $D \sim 2.5\ R_E$, which dramatically strengthened and thinned down to $D \sim 0.6\ R_E$ at the peak of the main phase of the storm of 6–10 April 2000, when the driving parameter of the inner tail field reached $W_{t1} \approx 9.7$. Note that the function (9) is probably the simplest one of many other possible choices with a greater or lesser flexibility, and it reproduces only the average trend of the tail current dynamics. The actual storm-time variation of the current sheet geometry can be more complicated, and its modeling would require a more uniform coverage by the data of the equatorial region in the range of distances 3–8 R_E. Even though our data set included a large number of synchronous observations, virtually all of them were located northward from the expected position of the equatorial current sheet, owing to the fixed position of the GOES spacecraft in the dipole magnetic coordinates at the latitude $\sim$4–10°.

[40] The redistribution of the model tail current along the X axis during a storm can be visualized by plotting profiles of the linear current density (net current per unit length of the tail) for consecutive phases of the event. Figure 2 displays such a sequence of profiles for the same storm of 6–10 April 2000. The profiles in each of the eight plots in Figure 2b represent the variation of the tail current density, integrated over the entire thickness of the current sheet within $|Z_{\mathrm{GSM}}| \leq 5\ R_E$ at $y = 0$, so that the plotted quantity is the current $J = \int j(x, z)dz$ in MA per 1 R_E of the tail length. The profiles in Figure 2b follow at 4-hour intervals, starting from the prestorm configuration at 12:50 UT of day 97 (6 April) and ending at 16:50 of day 98, well into the recovery phase. To help the reader

associate the profiles with the subsequent storm phases, the circled numbers in each plot correspond to the sequence of the time moments, displayed on the horizontal axis of the Dst variation in Figure 2a. The current profile in moment 1 corresponds to a prestorm distribution with the peak value of $J \sim 0.5\ \mathrm{MA}/R_E$ at $X \sim -9\ R_E$. Moment 2 corresponds to the storm's sudden commencement due to the arrival of a shock front with fast and dense solar wind, which resulted in an abrupt increase of the solar wind ram pressure from $\sim$1.5 nPa to 11 nPa. The most conspicuous effect is the formation of a second peak of the current at $X \sim -15\ R_E$ due to the larger sensitivity of the distant tail field (represented in the model by the term $t_2 \mathbf{B}_{\mathrm{T2}}$ in (5)) to the solar wind pressure, in comparison with the inner tail. In moment 3, the storm is well in progress, and the plot demonstrates a continued overall increase of the tail current, accompanied by its earthward shift and growth. At the peak of the main phase (moment 4), the tail current reaches its maximum and extends deep into the inner magnetosphere, with its inner edge located at unusually close geocentric distance of $\sim$3–4 R_E. At the recovery phase (moments 5–8), the current sheet recedes back into the tail and its overall magnitude gradually decreases. We note again that the actual instantaneous distributions of the storm-time current can be much more structured and complex, than the profiles in Figure 2. Most likely, their double-peaked shape reflects the fact that the model tail field includes only two terms in (5). It is in principle possible that adding more degrees of freedom and further extending the database would yield more sophisticated (either smoother or more structured) profiles of J with more interesting details. However, even at the present level of complexity, the model clearly reveals the most important effects: a quick initial response of the distant tail field to the upcoming compression front, followed by a more gradual strong increase and thinning of the innermost current sheet.

[41] The above described rise and decay of the storm-time currents dramatically impact the inner magnetospheric magnetic field structure, as illustrated in Figure 3. The six plots show noon-midnight configurations of the field lines, corresponding to six consecutive time moments of the storm of 6–10 April 2000, in the same order and using the same numbering as for the magnetotail current profiles in Figure 2 (moments 1 for 12:50 UT of day 97 and 8 for 16:50 of day 98 were omitted to avoid overcrowding of Figure 3). The field lines in each plot are spaced by 1° intervals of their foot point magnetic latitude, starting from $\Lambda = 50°$; for convenience of reading the plots, the lines corresponding to 55°, 60°, and 65° are drawn by dashed contours, and the line starting at 70° is dotted.

[42] Field line configuration in moment 2 corresponds to the moment of the storm sudden commencement. Owing to the faster and stronger response of the distant tail current to the abrupt sevenfold increase of the solar wind pressure, the initial stretching of the magnetic field begins at the outermost nightside boundary of the modeling region, with the formation of a neutral line at $x \sim -10\ R_E$. At closer distances (including synchronous orbit) the field remains quasi-dipolar, and the dayside polar cusps map at $\Lambda \sim 76°$. Four hours later (moment 3), as the Dst index drops below -200 nT, the configuration drastically changes: the overall compression of the magnetosphere is accompanied by a rapid equatorward shift of the dayside cusps to $\Lambda \approx 66–67°$
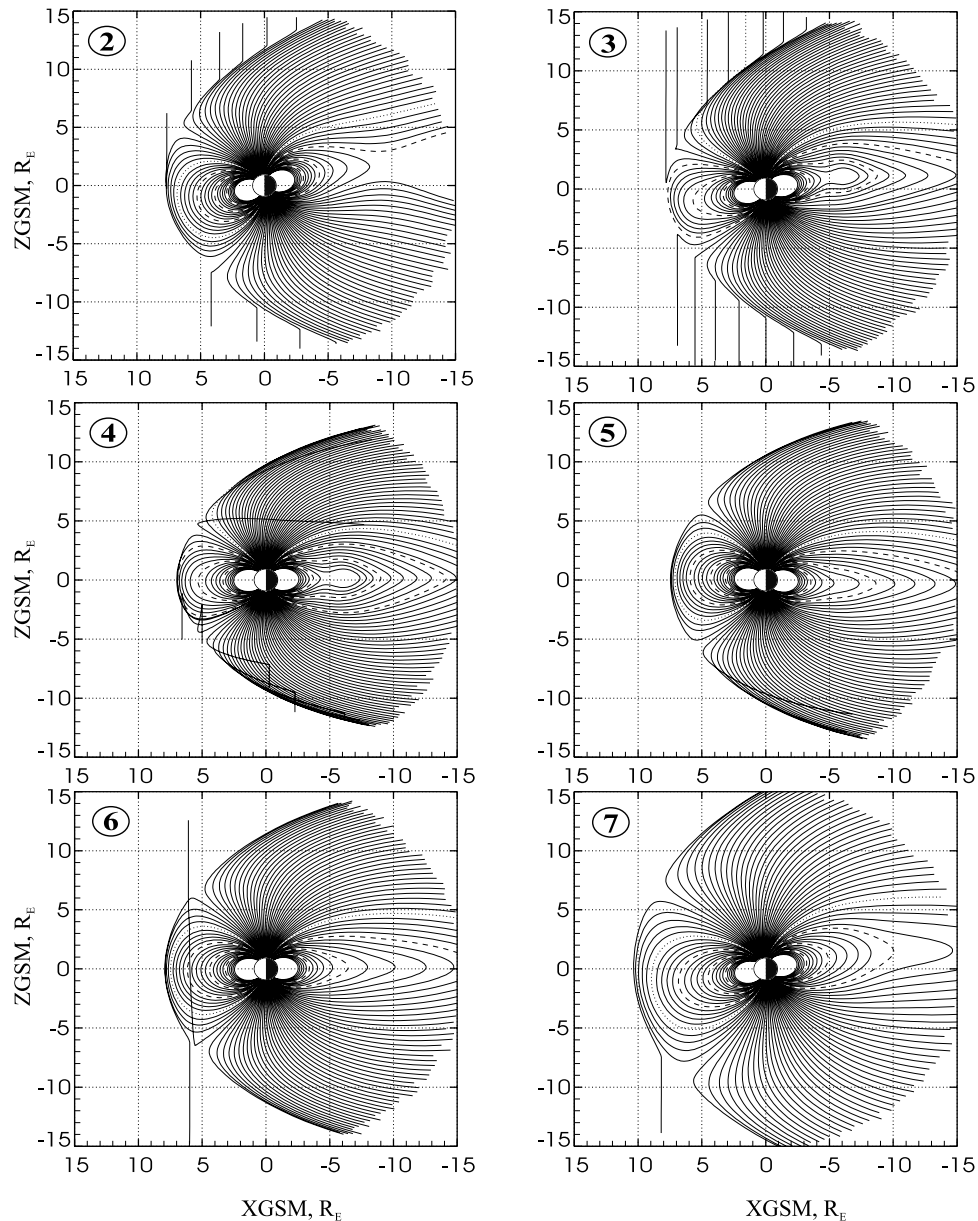
Figure 3. Six model field line configurations in the noon-midnight meridian plane, corresponding to moments 2–7 in Figure 2. Lines are plotted in 1° intervals of the foot point magnetic latitude, starting from 50°. Dashed lines correspond to the latitudes 55°, 60°, and 65°, and the dotted lines correspond to 70°.

and a severe stretching of the inner field on the nightside, so that the field lines become essentially tail-like even as close to Earth as at $X \sim -5 \ R_E$. In moment 4 (00:50 UT, day 98, $Dst \sim -300$ nT), the previously strong and southward IMF just started to rotate northward and the dayside cusps begin to recede poleward, but the nightside distortion is still increasing. At that time, the midnight field line with $\Lambda \sim 57°$ is stretched to $X \sim -7 \ R_E$, in reasonable agreement with the earlier result of TSK03 for the same event, based on the same data but simpler model approximations. Moment 5 corresponds to the early recovery phase of the storm, at which the magnetic configuration begins to gradually return back to normal. Owing mostly to a relatively quick decay of the region 1 field-aligned currents and northward IMF, the

polar cusps retreat to $\Lambda \sim 73-74°$, and the inner tail field becomes less stretched than in moment 4. This tendency persists in moment 6, and in the last plot (moment 7) the configuration is close to that before the storm.

5. Discussion

[43] In any modeling study based on a limited set of data, an important question is to what extent can one trust the model predictions. Ideally, a perfect test would be to compile an independent set of storm-time observations and evaluate the RMS deviation σ of the model field from the new data. A significantly larger value of σ would indicate a possible systematic bias in the model field, whose
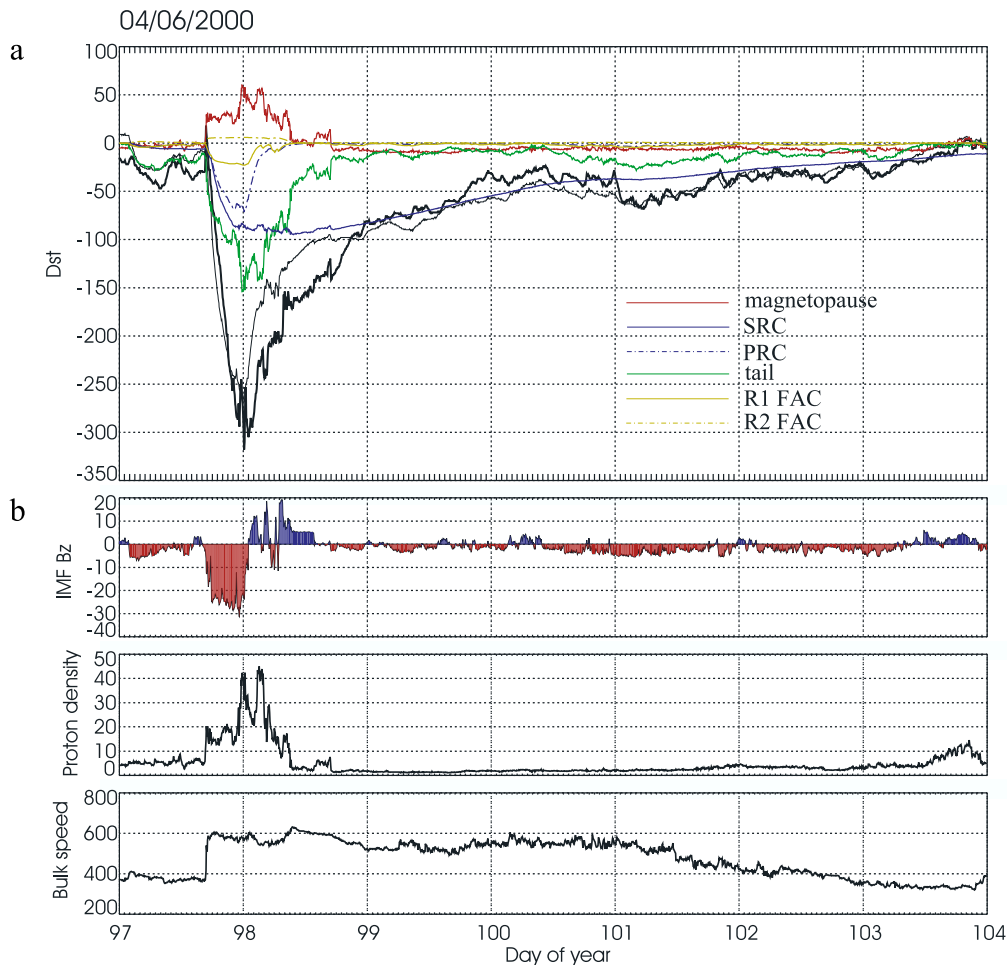
Figure 4. (a) Comparison of the observed *Dst* variation (thick black line) with that derived from the model field using (11) (thin black line). Colored lines correspond to individual contributions to the storm-time *Dst* from the six major sources of the external field. (b) Concurrent variation of the IMF B_z, solar wind proton density, and bulk speed. Intervals of the southward/northward IMF B_z are highlighted by red/blue.

nature could be further investigated by deriving a new set of model parameters from the new data set and comparing the two model fields in greater detail. The difference between the old and new values of the parameters would provide a measure of their uncertainties. This principle lies at the core of the "bootstrap" method [*Press et al.*, 1992; *Efron and Tibshirani*, 1993], in which the lack of truly independent data is circumvented by creating a family of "quasi-independent" subsamples from the original set by a random selection. That method was used here for estimating the uncertainties of the model parameters in Tables 1–3.

[44] T02b and TSK03 evaluated the overall quality of the model approximations by statistically comparing the observed and predicted values of three GSM components of the external field (i.e., with the Earth's main field subtracted). A similar estimate was made here for the present model, and the correlation coefficients (CC) for B_x, B_y, and B_z components were found equal to $R_x = 0.92$, $R_y = 0.83$, and $R_z = 0.92$, which appears just slightly better than for the TSK03 (0.91, 0.82, and 0.90, respectively). However, one should have in mind that the apparently marginal gain in the correlation coefficients and in the residual RMS deviation of

the model from data ($\sigma = 17.70$, as compared with $\sigma = 18.34$ of TSK03), should be viewed in the light of the fact that a large part of the discrepancy between the model and data is due to unpredictable fluctuations of the magnetospheric field, associated with the substorm explosions, release of plasmoids, large-scale oscillations caused by the flapping motion of the magnetopause and the tail current sheet, sawtooth events, etc. Among other sources of errors is a generally turbulent nature of the solar wind impact and related large-amplitude noise in the driving factors (e.g., variability of the IMF, ram pressure pulses, etc.), instrumental errors of the solar wind monitoring, errors due to a large distance between ACE/Wind and the magnetosphere (and hence inaccurate timing of the disturbance arrival).

[45] When estimating the agreement between the model and observed fields, it is more convenient to use a single vector correlation coefficient (VCC), instead of the three separate coefficients for B_x, B_y, and B_z. The VCC is defined only by the mutual orientation of the corresponding individual vectors in the set and hence is independent of the choice of the coordinate system. Formally, it has the same

Table 4. Comparison of the Observed and Model *Dst* Field for the 37-Storm (In-Sample) Modeling Data Set

Begin Date[a]	Min. *Dst*	CC	RMS Deviation	$\langle Dst^{(m)} - Dst \rangle$
10/22/1996	−122	0.934	10.7	8.3
01/10/1997	−84	0.886	11.1	4.9
04/10/1997	−91	0.890	12.2	4.7
04/21/1997	−100	0.924	9.5	3.4
05/01/1997	−80	0.853	10.7	7.5
05/15/1997	−125	0.949	11.8	−1.3
05/26/1997	−85	0.918	10.7	6.4
09/03/1997	−99	0.912	15.2	12.0
10/08/1997	−139	0.933	11.3	7.7
11/05/1997	−124	0.940	8.3	2.6
11/22/1997	−121	0.929	14.7	−6.7
02/17/1998	−119	0.966	10.0	4.0
03/10/1998	−118	0.921	9.2	0.9
05/02/1998	−264	0.914	23.6	−15.7
08/06/1998	−169	0.936	13.1	4.1
08/26/1998	−172	0.950	14.4	−3.6
09/24/1998	−213	0.931	19.3	−9.7
10/19/1998	−119	0.931	10.9	0.8
11/05/1998	−179	0.950	16.1	−9.1
11/13/1998	−123	0.924	29.1	−25.8
02/17/1999	−128	0.969	21.8	−15.2
02/28/1999	−93	0.947	10.5	−3.6
04/16/1999	−123	0.948	11.3	2.5
09/22/1999	−161	0.922	19.8	11.9
10/21/1999	−223	0.973	11.1	0.7
02/11/2000	−164	0.934	11.7	−1.5
04/06/2000	−318	0.943	21.4	3.3
04/15/2000	−93	0.910	12.2	8.7
04/24/2000	−78	0.832	15.6	11.7
07/15/2000	−338	0.836	40.2	−3.5
07/19/2000	−96	0.799	18.1	12.5
08/10/2000	−234	0.961	20.9	−15.8
09/12/2000	−66	0.949	6.8	3.8
09/15/2000	−196	0.892	17.9	5.1
10/02/2000	−184	0.969	12.1	−4.0
10/13/2000	−100	0.935	14.1	1.0
11/04/2000	−174	0.955	9.1	−4.1

[a]Dates are given in the format month/day/year.

properties and is defined in exactly the same way as the CC for the scalar data:

$$R_v = \frac{\sum_i \left(\mathbf{B}_i^{(obs)} - \langle \mathbf{B}^{(obs)} \rangle \right) \left(\mathbf{B}_i^{(mod)} - \langle \mathbf{B}^{(mod)} \rangle \right)}{\sqrt{\sum_i \left(\mathbf{B}_i^{(obs)} - \langle \mathbf{B}^{(obs)} \rangle \right)^2} \sqrt{\sum_i \left(\mathbf{B}_i^{(mod)} - \langle \mathbf{B}^{(mod)} \rangle \right)^2}},$$

(11)

except that the scalar quantities are replaced here by a set of vectors $\mathbf{B}_i^{(obs)}$ and $\mathbf{B}_i^{(mod)}$, representing the observed and model external fields, respectively. The angular brackets denote the averaging of the vectors over the entire set. The value of the When estimating the agreement between the model and observed fields, it is more convenient to use a single vector correlation coefficient (VCC), instead of the three separate coefficients for B_x, B_y, and B_z. The VCC between the present model and the 37-storm data set was found equal to $R_v = 0.90$.

[46] In view of the special importance of geosynchronous orbit, it is interesting to separately evaluate the model's performance in that region using 91,757 data records, contributed to our data set by GOES 8, 9, and 10 spacecraft. The respective values of R_x, R_y, R_z, and R_v were found in that case equal to 0.88, 0.87, 0.92, and 0.90.

[47] A simple check of the overall consistency of an external field model can be made by calculating the low-latitude disturbance at the Earth's surface for specific events and comparing it with the observed *Dst* variation. On the basis of the definition of the *Dst* index (SYM) as a local time average of the H component of the ground disturbance at low latitudes [e.g., *Iyemori*, 1990], the relationship between the model field $\mathbf{B}^{(mod)}$ at the Earth's surface and the expected (model-based) $Dst^{(m)}$ can be written as

$$Dst^{(m)} = \frac{\langle B_z^{(mod)} \rangle - A}{C},$$

(12)

where the mean low-latitude H component of the model external field at the Earth's surface $\langle B_z^{(mod)} \rangle$ is calculated in the solar-magnetic (SM) coordinates and the angular brackets denote averaging along the SM equator at $r = 1\ R_E$. The free term A is an unknown baseline, which, theoretically, should be close to the quiet-time value of $\langle B_z^{(mod)} \rangle$, so that $Dst^{(m)} = 0$ under quiet conditions. Using that assumption, the constant A was initially defined equal to −21.7 nT, the value of $\langle B_z^{(mod)} \rangle$ returned by the model for $P_d = 2$ nPa, IMF $B_y = B_z = 0$, and $W_i = 0$ ($i = 1, .., 6$). However, in that case the obtained values of $Dst^{(m)}$ were found to be systematically lower than the observed *Dst*, with the overall average bias equal to −11.1 nT. The parameter C in the denominator of (12) takes into account a contribution of the geomagnetically induced currents inside Earth during a storm. There is no universally accepted estimate for that parameter; according to *Langel and Estes* [1985], the induced ground field at low latitudes is in the range 24–29% of the external (inducing) field, which corresponds to the values of the parameter C in (12) between 0.77 and 0.81. However, that result was based only on quiet-time data with $|\text{Dst}| \leq 20$ nT, and it remains unclear whether it can be extrapolated to storms.

[48] In view of the ambiguity of the values of the parameters A and C in (12), it was eventually decided to determine them by minimizing the RMS deviation between the model-based $Dst^{(m)}$ and the actually observed *Dst* over the entire 55,008 5-min intervals, covering all the 37 events in our set. The best fit value of the residual baseline field A in (12) was found equal to −32.3 nT, that is, by −10.6 nT lower than the estimate −21.7 nT, obtained from the model prediction for the quiet-time input. The best fit induction coefficient C was found equal to 0.76, in a surprisingly close agreement with the above result by *Langel and Estes* [1985], as well as with the tentative estimate $C = 0.8$, used in the calculation of the corrected *Dst** of TSK03 and T02b.

[49] Figure 4 (top) shows the variation of the actual *Dst* (SYM) index (heavy black line) during the storm of 6–10 April 2000, and the corresponding model-based $Dst^{(m)}$ (thin black line), calculated from (12). Although in general the plots agree fairly well (CC = 0.943), $Dst^{(m)}$ peaks at −268 nT, which is 50 nT short of the actual value (−318 nT), and the model $Dst^{(m)}$ remains significantly higher than the actual *Dst* during the early recovery phase (until ~20:00 UT of day 98). In this example, the RMS difference between the model and actual *Dst* is 21.4 nT. In Figure 4 (top), the colored lines show the partial contributions to $Dst^{(m)}$ from individual current systems. As expected, the largest contributions come from the symmet-
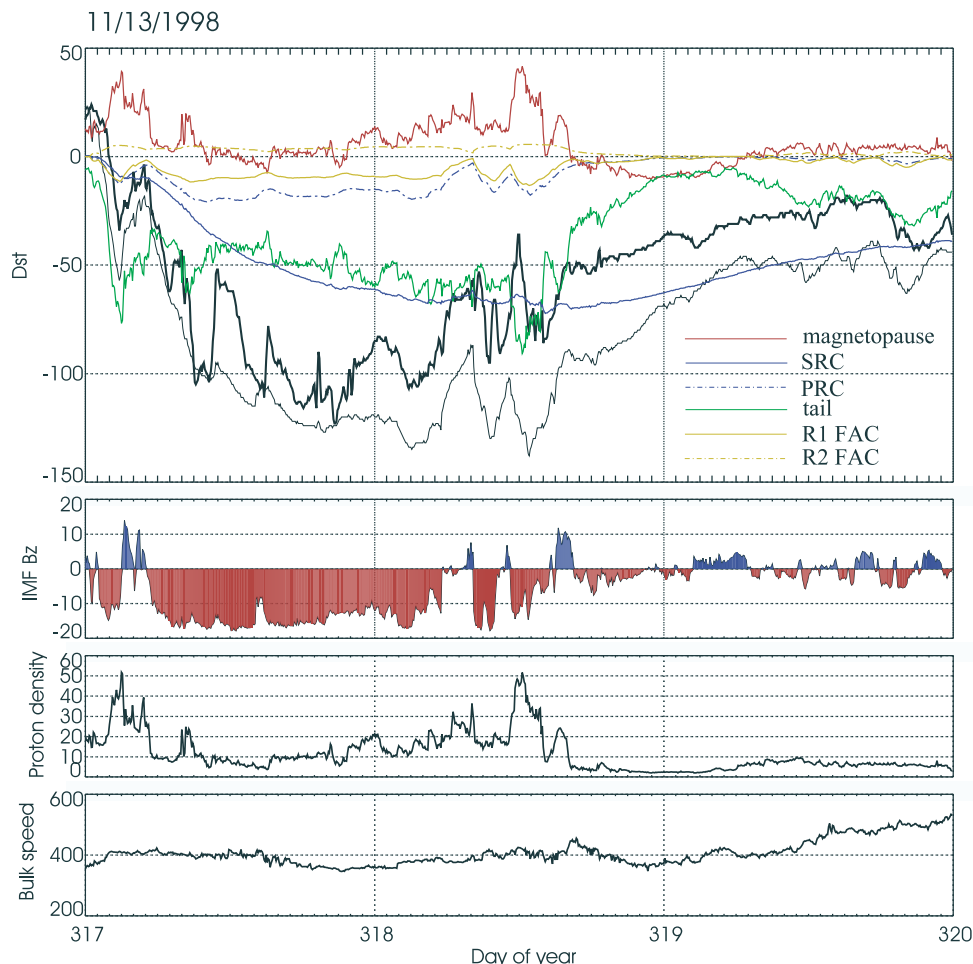
Figure 5. Same as Figure 4, but for the event of 13 November 1998.

rical ring current (SRC, blue line) and the near-Earth tail current (TC, green); note that the TC field actually dominates through the entire main phase, but rapidly subsides into background as the IMF turns northward, while the SRC field decreases much more slowly, owing to its much lower decay rate. The relatively large share of the cross-tail current in the ground *Dst* field was also found in a modeling study by *Alexeev et al.* [1996], while *Ganushkina et al.* [2004] argued that the tail current contribution dominated over that of the ring current only during moderate storms.

[50] As already noted, even though the total partial ring current (PRC) is comparable to that of the SRC and in many cases exceeds it at the peak of the main phase, it yields a relatively small contribution to the ground *Dst* field (dash-dotted blue line). This is due to the fact that the north-south magnetic field produced by the westward near-equatorial part of the PRC is largely offset in the dawn sector by the opposite effect of the field-aligned closure currents. As a result, the associated equatorial H component varies with local time between large positive and negative values, which cancel each other in the average. The largest near-equatorial magnetic depression associated with the PRC is concentrated at distances $2 \leq R \leq 3$ R_E at postdusk MLT hours (see TSK03, Figures 10 and 12 and relevant discussion).

[51] For the same reason, the model $Dst^{(m)}$ gains relatively small contribution from the field-aligned currents (yellow lines), even though, locally, their ground magnetic effect at low latitudes can be quite large (up to $\sim$100–150 nT) around noon and midnight. The red line in Figure 4 corresponds to the contribution to *Dst* from the magneto-pause currents. Note that we subtracted from all the partial fields shown in Figure 4 their average quiet-time values; in other words, the plot reflects only storm-time effects in the *Dst* field. This explains why the plotted magnetopause field is close to zero before the storm sudden commencement. During the late recovery phase that field even becomes negative, manifesting the unusually low ram pressure of the solar wind in the wake of the disturbance.

[52] We compared the observed and model-based variation of the *Dst* index for all 37 events in our data set, with the results summarized in Table 4. For each of the 37 storms, Table 4 gives the values of the observed minimum *Dst*, correlation coefficients, RMS difference, and the average bias of $Dst^{(m)}$. Most of the individual CC vary in the range 0.85–0.95, and the corresponding RMS deviation varies between 10 and 40 nT. The cumulative CC and RMS deviation, calculated from the entire 37-storm set, were found equal to 0.92 and 15.8 nT, respectively. The largest negative bias of $Dst^{(m)}$, equal to −25.8 nT, was found for the storm of 13–15 November 1998. Figure 5 displays the dynamics of the actual and model-based *Dst* index for that event, as well as the concurrent solar wind conditions, in the same format as in Figure 4. A characteristic feature of that

Table 5. Comparison of the Observed and Model *Dst* Field for the 19-Storm (Out-of-Sample) Set

Begin Date	Min. *Dst*	CC	RMS Deviation	$\langle Dst^{(m)} - Dst \rangle$
06/24/1998	−120	0.874	12.8	1.3
10/28/2000	−121	0.959	15.8	−12.4
11/24/2000	−127	0.951	14.8	−5.8
03/19/2001	−165	0.965	10.1	0.9
03/27/2001	−434	0.906	34.2	−4.6
04/11/2001	−275	0.927	25.0	−13.9
04/17/2001	−119	0.907	11.9	0.2
04/21/2001	−104	0.973	7.6	−0.6
08/17/2001	−131	0.795	19.0	0.7
09/21/2001	−188	0.920	15.3	5.1
10/19/2001	−212	0.976	11.7	−2.0
10/27/2001	−150	0.954	12.5	7.3
03/23/2002	−114	0.944	14.0	7.9
04/17/2001	−182	0.909	16.4	−0.6
05/11/2002	−110	0.898	14.2	−2.5
05/23/2002	−113	0.914	19.3	13.4
09/03/2002	−167	0.958	9.7	−1.8
09/30/2002	−154	0.952	16.8	−12.8
11/17/2002	−126	0.922	12.2	−5.7

storm was a relatively long (∼24 hours) interval of large and steady southward IMF B_z, and that was also the case for other storms that yielded large negative bias of $Dst^{(m)}$. According to our simple model (1)–(6), in such cases the tail field should have increased and remained in this higher-energy state until the end of the period of enhanced driving. In contrast, the actual evolution of the storm-time tail current is rather different: this is an essentially nonlinear process, including intermittent buildups of the magnetic energy and subsequent fast reconfigurations. Our model ignores all the explosive processes by representing the tail dynamics merely as a result of the competition between the external injection and a steady internal dissipation of the tail magnetic energy. That can result in an overestimate of the driving effect and/or underestimate of the role of the rapid relaxation of the magnetotail field via substorms, which is particularly evident from the actual *Dst* variation in the beginning (day 317) of the storm in Figure 5. There were at least 4 rapid and large positive excursions of the actual *Dst*, associated with substorm expansions, but none of them was adequately replicated in the variation of $Dst^{(m)}$. The rapid relaxations of the stressed tail field were addressed in a recent empirical simulation by *Freeman and Morley* [2004].

[53] Many other factors could also contribute to the discrepancies between the model and observed *Dst*. The actual dynamics of the ring current, the second major contributor to *Dst*, is more complex than in our model. In particular, its dissipation rate can significantly vary not only from one storm to another, but also in the course of a single storm [*Valdivia et al.*, 1996], which means that the corresponding coefficient r in (3) should actually be

Figure 6. Same as Figure 4, but for the event of 3 September 2002.

treated as a variable parameter [*Gonzalez et al.*, 1994, and references therein].

[54] Another important factor is the initial state of the magnetosphere before the storm. Our model assumes that the efficiency of the external driving depends only on the current state of the solar wind and IMF and hence ignores the role of the prestorm conditions. However, as demonstrated by *Thomsen et al.* [2003], the magnitude of a storm depends not only on the intensity of the ongoing driving during the active phase of a disturbance, but also on the "preconditioning" of the magnetosphere, for example, by a prolonged interval of northward IMF.

[55] In a sense, the results given in Table 4 should be viewed as an "in-sample" test, since the comparison of the observed and model *Dst* was made for the same set of 37 events that provided the magnetospheric data, used in the derivation of the model. It is interesting to make a similar consistency check, but using "out-of-sample" data. An effort is currently underway to extend our 37-storm set by adding more events, from the end of 2000 to the most recent storms. Table 5, identical in format to Table 4, shows the results of calculating and comparing $Dst^{(m)}$ with the observed *Dst* for a set of 19 newly compiled major events in 2000–2002. In general, all the results are very similar to those for the "in-sample" comparison in Table 4. The cumulative CC, RMS deviation, and the bias between the model and observed *Dst* over all 19 storms were found equal to 0.92, 16.6 nT, and −1.6 nT, respectively. Figure 6 shows a result of the "out-of-sample" comparison for the storm of Sep. 3, 2002. In that example, the CC, RMS deviation, and bias are 0.96, 9.7 nT, and −1.8 nT, respectively.

6. Summary and Outlook

[56] In this paper we described a dynamical data-based model of the inner magnetosphere, representing its structure and temporal variation during geomagnetic storms. The model uses spacecraft data taken during 37 events in 1996–2000 and approximates the magnetic field as a sum of contributions from all major external current systems, each of which evolves in time according to its own mode of response to the solar wind driving, saturation threshold, and relaxation timescale. The approach is based on representing the dynamics of each source as a result of the competition between the external driving and internal dissipation. All the quantitative characteristics of the model current systems, including their quiet-time magnitudes, geometrical parameters, variables entering in the solar wind driving functions, decay timescales, and saturation thresholds, were derived by minimizing the RMS deviation of the model field from the entire 37-storm data set. The relaxation/response timescales of the individual field sources were found to largely differ between each other, from as large as ∼30 hours for the symmetrical ring current to only ∼50 min for the region 1 Birkeland current. The total magnitudes of the currents were also found to dramatically vary in the course of major events, with the peak values as large as 5−8 MA for the symmetric ring current and region 1 field-aligned current. At the peak of the main phase, the total partial ring current can largely exceed the symmetric one, reaching ∼10 MA and even more, but it quickly subsides as the external solar wind driving disappears, with the relaxation time ≤2 hours. The tail current dramatically increases during the main phase and shifts earthward, so that the peak current concentrates at unusually close distances ∼4−6 R_E. This is accompanied by a significant thinning of the current sheet and strong tailward stretching of the inner geomagnetic field lines. As an independent consistency test, we calculated the expected *Dst* variation on the basis of the model output at Earth's surface and compared it with the actual observed *Dst*. A good agreement (cumulative correlation coefficient R = 0.92) was found, in spite of that ∼90% of the spacecraft data used in the fitting were taken at synchronous orbit and beyond, while only 3.7% of those data came from distances $2.5 \leq R \leq 4 \ R_E$. Our results also reveal the storm-time dynamics of individual contributions of principal external field sources to the ground magnetic disturbance. In this regard, the tail current and the symmetric ring current are the most important contributors to the *Dst* index. In most cases, the tail field even exceeds that of the ring current during the main phase, but then quickly subsides, leaving the symmetrical ring current as the dominant source through the rest of the recovery phase. The obtained results demonstrate the possibility to develop a dynamical model of the magnetic field, based on magnetospheric and interplanetary data and allowing one to reproduce and forecast the entire process of a geomagnetic storm, as it unfolds in time and space.

[57] Future efforts in this direction should be focused on including substorm effects in the models, with the goal to describe and predict the explosive reconfigurations of the field. As already noted above, an interesting semiempirical approach was proposed recently by *Freeman and Morley* [2004], based on simple "minimal substorm" model of the external driving and internal relaxation of the stressed magnetotail. Another potentially promising approach would be to include in the modeling the preconditioning of the magnetosphere before the southward turning of the IMF [*Thomsen et al.*, 2003].

References

Alexeev, I. I., E. S. Belenkaya, V. V. Kalegaev, Y. I. Feldstein, and A. Grafe (1996), Magnetic storms and magnetotail currents, *J. Geophys. Res.*, *101*, 7737.

Baker, D. N., A. J. Klimas, R. L. McPherron, and J. Büchner (1990), The evolution from weak to strong geomagnetic activity: An interpretation in terms of deterministic chaos, *Geophys. Res. Lett.*, *17*, 41.

Burton, R. K., R. L. McPherron, and C. T. Russell (1975), An empirical relationship between interplanetary conditions and *Dst*, *J. Geophys. Res.*, *80*, 4204.

Caan, M. N., R. L. McPherron, and C. T. Russell (1975), Substorm and interplanetary magnetic field effects on the geomagnetic tail lobes, *J. Geophys. Res.*, *80*, 191.

Collier, M. R., J. A. Slavin, R. P. Lepping, K. Ogilvie, and A. Szabo (1998), Multispacecraft observations of sudden impulses in the magnetotail caused by solar wind pressure discontinuities: Wind and IMP 8, *J. Geophys. Res.*, *103*, 17,293.

Dremukhina, L. A., Y. I. Feldstein, I. I. Alexeev, V. V. Kalegaev, and M. E. Greenspan (1999), Structure of the magnetospheric magnetic field during magnetic storms, *J. Geophys. Res.*, *104*, 28,351.

Efron, B., and R. Tibshirani (1993), *An Introduction to the Bootstrap*, CRC Press, Boca Raton, Fla.

Fairfield, D. H., and J. Jones (1996), Variability of the tail lobe field strength, *J. Geophys. Res.*, *101*, 7785.

Freeman, M. P., and S. K. Morley (2004), A minimal substorm model that explains the observed statistical distribution of times between substorms, *Geophys. Res. Lett.*, *31*, L12807, doi:10.1029/2004GL019989.

Ganushkina, N. Y., T. I. Pulkkinen, M. V. Kubyshkina, H. J. Singer, and C. T. Russell (2004), Long-term evolution of magnetospheric current systems during storms, *Ann. Geophys.*, *22*, 1317.

Gonzalez, W. D., J. A. Joselyn, Y. Kamide, H. W. Kroehl, G. Rostoker, B. T. Tsurutani, and V. M. Vasyliunas (1994), What is a geomagnetic storm?, *J. Geophys. Res.*, *99*, 5771.

Horton, W., and I. Doxas (1996), A low-dimensional energy conserving state space model for substorm dynamics, *J. Geophys. Res.*, *101*, 27,223.

Iyemori, T. (1990), Storm-time magnetospheric currents inferred from mid-latitude geomagnetic field variations, *J. Geomagn. Geoelectr.*, *42*, 1249.

Kaufmann, R. L. (1987), Substorm currents: Growth phase and onset, *J. Geophys. Res.*, *92*, 7471.

Klimas, A. J., D. N. Baker, D. A. Roberts, D. H. Fairfield, and J. Büchner (1992), A nonlinear dynamical analogue model of geomagnetic activity, *J. Geophys. Res.*, *97*, 12,253.

Langel, R. A., and R. H. Estes (1985), Large-scale, near-Earth magnetic fields from external sources and the corresponding induced internal field, *J. Geophys. Res.*, *90*, 2487.

Liemohn, M. W., J. U. Kozyra, M. F. Thomsen, J. L. Roeder, G. Lu, J. E. Borovsky, and T. E. Cayton (2001), Dominant role of the asymmetric ring current in producing the stormtime *Dst*, *J. Geophys. Res.*, *106*, 10,883.

Lui, A. T. Y., and D. C. Hamilton (1992), Radial profiles of quiet time magnetospheric parameters, *J. Geophys. Res.*, *97*, 19,325.

Maltsev, Y. P. (2004), Points of controversy in the study of magnetic storms, *Space Sci. Rev.*, *110*, 227.

McPherron, R. L. (1972), Substorm related changes in the geomagnetic tail: The growth phase, *Planet. Space Sci.*, *20*, 1521.

Press, W. H., S. A. Teukolsky, W. T. Vetterling, and B. P. Flannery (1992), *Numerical Recipes*, 2nd ed., Cambridge Univ. Press, New York.

Shue, J.-H., et al. (1998), Magnetopause location under extreme solar wind conditions, *J. Geophys. Res.*, *103*, 17,691.

Skoug, R. M., et al. (2003), Tail-dominated storm main phase: 31 March 2001, *J. Geophys. Res.*, *108*(A6), 1259, doi:10.1029/2002JA009705.

Temerin, M., and X. Li (2002), A new model for the prediction of *Dst* on the basis of the solar wind, *J. Geophys. Res.*, *107*(A12), 1472, doi:10.1029/2001JA007532.

Thomsen, M. F., J. E. Borovsky, R. M. Skoug, and C. W. Smith (2003), Delivery of cold, dense plasma sheet material into the near-Earth region, *J. Geophys. Res.*, *108*(A4), 1151, doi:10.1029/2002JA009544.

Tsyganenko, N. A. (1991), Methods for quantitative modeling of the magnetic field from Birkeland currents, *Planet. Space Sci.*, *39*, 641.

Tsyganenko, N. A. (1996), Effects of the solar wind conditions on the global magnetospheric configuration as deduced from data-based field models, in *Proceedings of the Third International Conference on Substorms (ICS-3), Versailles, France, 12–17 May 1996*, edited by E. Rolfe and B. Kaldeich, *Eur. Space Agency Spec. Publ.*, *ESA-SP*, *389*, p. 181.

Tsyganenko, N. A. (2000a), Solar wind control of the tail lobe magnetic field as deduced from Geotail, AMPTE/IRM, and ISEE-2 data, *J. Geophys. Res.*, *105*, 5517.

Tsyganenko, N. A. (2000b), Modeling the inner magnetosphere: The asymmetric ring current and region 2 Birkeland currents revisited, *J. Geophys. Res.*, *105*, 27,739.

Tsyganenko, N. A. (2002a), A model of the near magnetosphere with a dawn-dusk asymmetry: 1. Mathematical structure, *J. Geophys. Res.*, *107*(A8), 1179, doi:10.1029/2001JA000219.

Tsyganenko, N. A. (2002b), A model of the near magnetosphere with a dawn-dusk asymmetry: 2. Parameterization and fitting to observations, *J. Geophys. Res.*, *107*(A8), 1176, doi:10.1029/2001JA000220.

Tsyganenko, N. A., H. J. Singer, and J. C. Kasper (2003), Storm-time distortion of the inner magnetosphere: How severe can it get?, *J. Geophys. Res.*, *108*(A5), 1209, doi:10.1029/2002JA009808.

Valdivia, J. A., A. S. Sharma, and K. Papadopoulos (1996), Prediction of magnetic storms by nonlinear models, *Geophys. Res. Lett.*, *23*, 2899.

————————————

M. I. Sitnov, Institute for Research in Electronics and Applied Physics, University of Maryland, College Park, MD 20742, USA. (sitnov@umd.edu)

N. A. Tsyganenko, Universities Space Research Association and Laboratory for Solar and Space Physics, NASA Goddard Space Flight Center, Code 612.3, Greenbelt, MD 20771, USA. (nikolai.tsyganenko@gsfc.nasa.gov)